

Letter

## All-Solid-State Batteries with Thick Electrode Configurations

Yuki Kato, Shinya Shiotani, Keisuke Morita, Kota Suzuki, Masaaki Hirayama, and Ryoji Kanno

*J. Phys. Chem. Lett.*, **Just Accepted Manuscript** • DOI: 10.1021/acs.jpcllett.7b02880 • Publication Date (Web): 17 Jan 2018

Downloaded from <http://pubs.acs.org> on January 17, 2018

### Just Accepted

"Just Accepted" manuscripts have been peer-reviewed and accepted for publication. They are posted online prior to technical editing, formatting for publication and author proofing. The American Chemical Society provides "Just Accepted" as a free service to the research community to expedite the dissemination of scientific material as soon as possible after acceptance. "Just Accepted" manuscripts appear in full in PDF format accompanied by an HTML abstract. "Just Accepted" manuscripts have been fully peer reviewed, but should not be considered the official version of record. They are accessible to all readers and citable by the Digital Object Identifier (DOI®). "Just Accepted" is an optional service offered to authors. Therefore, the "Just Accepted" Web site may not include all articles that will be published in the journal. After a manuscript is technically edited and formatted, it will be removed from the "Just Accepted" Web site and published as an ASAP article. Note that technical editing may introduce minor changes to the manuscript text and/or graphics which could affect content, and all legal disclaimers and ethical guidelines that apply to the journal pertain. ACS cannot be held responsible for errors or consequences arising from the use of information contained in these "Just Accepted" manuscripts.



ACS Publications

# All-solid-state Batteries with Thick Electrode Configurations

*Yuki Kato,<sup>†‡\*</sup> Shinya Shiotani,<sup>‡§</sup> Keisuke Morita,<sup>‡</sup> Kota Suzuki,<sup>§</sup> Masaaki Hirayama,<sup>§</sup> Ryoji Kanno<sup>§</sup>*

<sup>†</sup>Toyota Motor Europe NV/SA, Hoge Wei 33, 1930 Zaventem, Belgium.

<sup>‡</sup>Toyota Motor Corporation, 1200 Mishuku, Susono, Shizuoka, 410-1107 Japan.

<sup>§</sup>Department of Chemical Science and Engineering, School of Materials and Chemical Technology, Tokyo Institute of Technology, 4259 Nagatsuta, Midori, Yokohama, 226-8502 Japan.

## AUTHOR INFORMATION

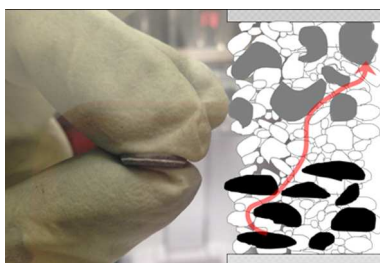
### Corresponding Author

\*Yuki Kato (yuki\_katoh@mail.toyota.co.jp).

## ABSTRACT

We report the preparation of thick electrode all-solid-state lithium-ion cells in which a large geometric capacity of  $15.7 \text{ mAh cm}^{-2}$  was achieved at room temperature using a  $600 \text{ }\mu\text{m}$ -thick cathode layer. The effect of ionic conductivity on the discharge performance was then examined using two different materials for the solid electrolyte. Furthermore, important morphological information regarding the tortuosity factor was electrochemically extracted from the capacity-current data. The effect of tortuosity on cell performance was also quantitatively discussed.

## TOC GRAPHIC



Increasing the thickness of an electrode is an attractive option for improving the energy densities of batteries, as it minimizes the relative volume of inactive components, such as the current collector and the separator.<sup>1–5</sup> However, it leads to challenges in terms of power characteristics due to limited ion or electron transport in thick electrodes. To date, the power capabilities of lithium-ion batteries containing thick electrodes have been improved by the incorporation of three-dimensional structured substrates, such as aligned carbon, metal foil, and porous carbon.<sup>2–4</sup> However, in the high current density region, the rate capabilities of thick electrode systems remain limited by ion diffusion in the liquid electrolyte.<sup>4,5</sup> Indeed, the low transference number of lithium ions ( $t_{\text{Li}^+} < 0.4$ ) results in a concentration gradient of lithium ions across the system during charge/discharge.<sup>6,7</sup>

As such, all-solid-state batteries can be considered an alternative option for thick electrode systems, as the transference number of inorganic solid electrolytes is almost unity. In addition, a number of solid electrolytes exhibit higher ionic conductivities than liquid electrolytes, leading to the production of high power all-solid-state batteries that exhibit improved rate capabilities compared to liquid electrolyte-based lithium-ion batteries.<sup>8</sup> Although all-solid-state batteries with thick electrode configurations have been reported,<sup>8,9</sup> the quantitative analysis of ionic transport, such as the effects of ionic conductivity and morphology, have not yet been examined. Thus, we herein report all-solid-state batteries exhibiting higher surface capacities than previously reported systems (Fig. S1).<sup>8,10–12</sup> In addition, a systematic investigation of the effects of ionic conductivity and electrode morphology on the discharge performances of such systems is reported.

A schematic representation of the cell employed herein is shown in Figure 1, and details regarding the prepared solid electrolytes exhibiting different ionic conductivities are provided in Table 1 (also see Figures S3–S5 and the Supporting Information for experimental procedures and additional information).<sup>13–15</sup>  $\text{LiNbO}_3$ -coated  $\text{LiCoO}_2$ <sup>16</sup> and graphite were selected for the cathode and the anode, respectively. As indicated in Tables 2 and 3, the composite electrodes were prepared using a mixture of powders to give a separator layer ( $L_s$ ) thickness of 100  $\mu\text{m}$ , in addition to a range of electrode layer thicknesses. A higher specific energy and energy density were obtained with the thicker electrode (Fig. S2).

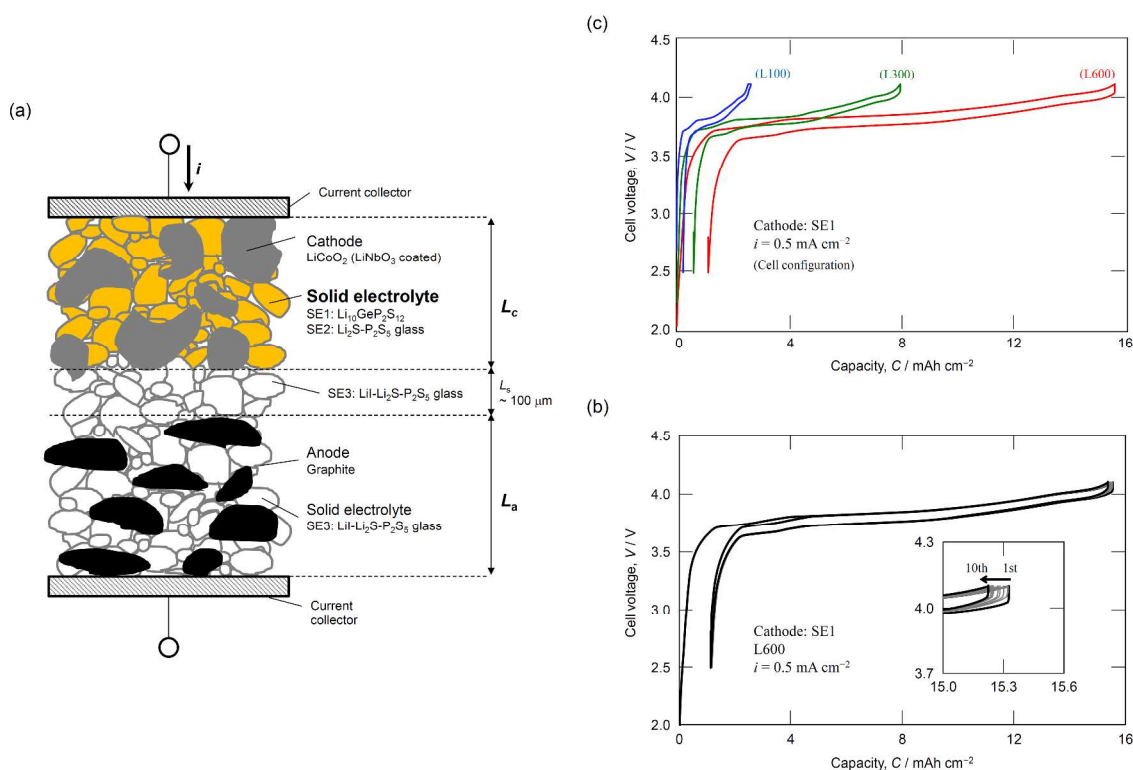


**Figure 1.** (a) Schematic representation of the experimental setup. (b) The charge/discharge capability of the thick electrode configuration. (c) Cycling performance of the L600 configuration.

**Table 1.** Details of the solid electrolytes employed herein

solid electrolyte	composition	ionic conductivity ( $\kappa/\text{mS cm}^{-1}$ )
SE1	$\text{Li}_{10}\text{GeP}_2\text{S}_{12}$	3.2
SE2	$75\text{Li}_2\text{S}-25\text{P}_2\text{S}_5$	0.28
SE3	$30\text{LiI}-70(0.75\text{Li}_2\text{S}-0.25\text{P}_2\text{S}_5)$	1.2

**Table 2.** The powder mixtures employed for preparation of the cathode and anode layers

material	density ( $\rho/\text{g cm}^{-3}$ )	mass fraction in electrode (wt%)		volume fraction in electrode (vol%)	
		cathode layer	anode layer	cathode layer	anode layer
$\text{LiCoO}_2$ ( $\text{LiNbO}_3$ coated)	5.05	61	-	38.1	-
Acetylene black	2.00	3	-	4.8	-
Solid electrolyte	2.00	36	54	57.1 ( $\epsilon=0.57$ )	57 ( $\epsilon=0.57$ )
Graphite	2.27	-	46	-	43

**Table 3.** Properties of the prepared cathode and anode layers

configuration	cathode layer		anode layer		capacity (cathode limited) ( $\text{C}/\text{mAh cm}^{-2}$ )
	thickness ( $L_c/\mu\text{m}$ )	LCO loading ( $M_{\text{LCO}}/\text{mg cm}^{-2}$ )	thickness ( $L_a/\mu\text{m}$ )	graphite loading ( $M_g/\text{mg cm}^{-2}$ )	

L75	~75	14.5	~66	6.4	2.00
L100	~100	19.3	~88	8.6	2.64
L125	~125	24.1	~109	10.7	3.30
L150	~150	28.9	~131	12.8	3.96
L200	~200	38.6	~174	17.1	5.29
L250	~250	48.2	~219	21.4	6.60
L300	~300	57.7	~262	25.6	7.93
L600	~600	115.4	~524	51.3	15.7

The charge-discharge curves obtained at  $0.5 \text{ mA cm}^{-2}$  using SE1 as the solid electrolyte are shown in Figure 1(b), where it is apparent that the theoretical capacity was successfully cycled at this current density even for the thick electrode configuration of L600 ( $\text{LiCoO}_2$  mass loading =  $115.4 \text{ mg cm}^{-2}$ ). In addition, in the constant current mode, the charge capacity reached >95% of the theoretical capacity, while the discharge capacity reached 93%, thereby indicating the potential of this system. Figure 1(c) shows the cycling test of the L600 configuration at  $0.5 \text{ mA cm}^{-2}$ . A good cyclability (>99% capacity after 10 cycles with a charge/discharge efficiency of ~100%) was exhibited under these conditions, thereby indicating that the change in volume was accommodated over a minimum of 10 cycles. The relatively low efficiency observed for the first cycle may be due to the reaction generating a passivation layer at the anode/solid-electrolyte interface. In addition, the small but gradually increasing overpotential observed during cycling may originate from side reactions at the interface between the cathode material and the carbon additives.<sup>10,17</sup> This could be suppressed by minimizing the amount of carbon additives employed. These results indicate that an electrode design that balances electron

conductivity and durability may be required for applications requiring greater cycle numbers (e.g., >1000 cycles).

Figure 2(a) shows the variation in the charge-discharge characteristics of the L600 and L300 configurations at  $0.5 \text{ mA cm}^{-2}$  relative to the specific capacity of  $\text{LiCoO}_2$ . Evolution of the overpotential was also observed upon increasing the electrode thickness, thereby indicating energy loss due to ionic transport in the electrode layer. Although a plateau in the potential was observed for the L300 configuration that corresponded with the stage structure of graphite, a smoother slope was observed for the L600 configuration, with the differential constant ( $\Delta V/\Delta C$ ) at  $\sim 3.8 \text{ V}$  being a good indication of this (see the right-hand panel of Figure 2(a)). Indeed, this difference between the two configurations reflects the particle distributions at different states of charge across the electrodes due to the required overpotential for mass transport.

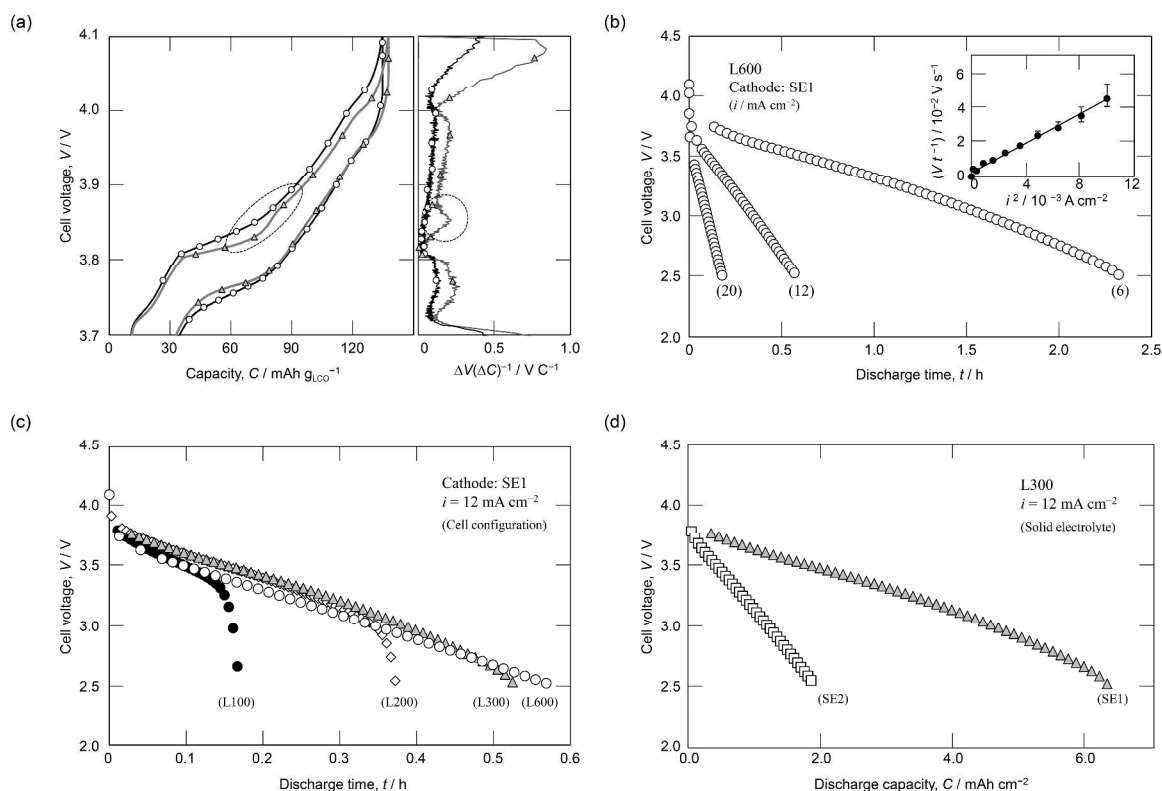




**Figure 2.** Charge/discharge curves of the all-solid-state cells. (a) The charge/discharge capability of the thick electrode configuration. The discharge behavior was investigated by varying (b) the current density, (c) the electrode thickness, and (d) the ionic conductivity of the cathode layer.

Figure 2(b) shows the discharge curves of the L600 cell prepared using SE1 at different discharge current densities ( $i$ ). Below  $i=6 \text{ mA cm}^{-2}$ , the cell exhibited an almost theoretical capacity, while the discharge capacity ( $C$ ) of  $13.9 \text{ mAh cm}^{-2}$  at  $i=6 \text{ mA cm}^{-2}$  represented 88% of its theoretical capacity. In addition, the relatively straight discharge curves observed where  $i > 6 \text{ mA cm}^{-2}$  indicate that the reaction is limited by an ohmic potential drop in the electrolyte layer to a greater extent than diffusion in the active materials. The operation of a  $\text{LiCoO}_2/\text{graphite}$  system at current densities  $>50 \text{ mA cm}^{-2}$  with a thin electrode layer (i.e.,  $25 \mu\text{m}$  thickness)<sup>8</sup> indicates that the active material particles can respond rapidly at current densities  $<50 \text{ mA cm}^{-2}$ . Indeed, in the case of a thick electrode system, this is feasible, as the current density per particle decreases with increasing thickness. As such, the reaction of our battery can be understood using the reaction zone model proposed by Newman *et al.*,<sup>18</sup> which is valid for a system based on highly diffusive active materials. Since the effective electron conductivity ( $\sigma_{\text{eff}_e}=0.3 \text{ S cm}^{-1}$ ,  $\sigma_{\text{eff}_a}=0.7 \text{ S cm}^{-1}$ ) was significantly larger than the ionic conductivity of a solid electrolyte ( $\kappa$ ), the potential drop is considered to originate from ionic transport in our system. The voltage profile of the half-cell at the ohmic limit can therefore be expressed as indicated in Eq. 1:

$$V = U^{\theta} - R_o i - \frac{t}{q \kappa_{eff}} i^2 \quad (Eq. 1)$$

where  $U^{\theta}$ ,  $R_o$ ,  $q$ ,  $\kappa_{eff}$ , and  $t$  are the open circuit potential of the active material in the charged state, the high frequency resistance, the capacity density of the composite electrode, the effective ionic conductivity of the composite electrode, and the time, respectively. In addition, the relationship  $\frac{t}{q \kappa_{eff}} i^2 = \left[ (ti/q) \cdot 1/\kappa_{eff} \right] \times i$  represents the ohmic potential drop evolution during charge-discharge, where  $(ti/q)$  represents the coordination of the reaction zone front, and  $(i/q)$  is the velocity.<sup>18</sup> Incorporation of the volume fraction of the electrolyte  $\varepsilon$  and the tortuosity factor  $\tau$  gives the effective conductivity of the composite electrode:

$$\kappa_{eff} = \frac{\varepsilon}{\tau} \kappa \quad (Eq. 2)$$

As both Eqs. 1 and 2 incorporate the morphological parameter of the tortuosity factor, this parameter can be estimated by analyzing the discharge curves. At the ohmic limit, the slope of the discharge curves includes direct information regarding the morphology of the all-solid-state cell, the estimation of which is usually challenging using non-destructive methods. Equation 1 can therefore be modified to give the full cell model, and upon considering the direction of current, the voltage behavior of the full cell at the ohmic limit can be expressed as Eq. 3:

$$V = U_c^{\theta} - U_a^{\theta} - R_o i - \left( \frac{1}{q_c \kappa_{effc}} + \frac{1}{q_a \kappa_{effa}} \right) i^2 \times t \quad (Eq. 3)$$

where  $c$  and  $a$  denote the values corresponding to the cathode and the anode, respectively. Thus, Eq. 3 indicates that the slope of the discharge curve is proportional to the square of the applied current density. The ratios of the slopes shown in Figure 2(b) correspond with the ratios of the

squared currents (i.e., slopes = -0.52, -2.07, and -6.22 at  $i=6, 12$ , and  $20 \text{ mA cm}^{-2}$ , respectively).

In addition, the inset of Figure 2(b) shows the relationship between the slope of the discharge curve and the squared current, with the relatively straight lines produced indicating that the cells are at the ohmic limit. Furthermore, the slope shown in the inset of Figure 2(b) corresponds with the value of  $\left(\frac{1}{q_c \kappa_{effc}} + \frac{1}{q_a \kappa_{effa}}\right)$  for the SE1 system.

Moreover, Figure 2(c) shows the discharge curves at  $i=12 \text{ mA cm}^{-2}$  for different electrode thicknesses (i.e., L100, L200, and L600). In the case of the thinnest electrode configuration (L100), >80% of the capacity was discharged, indicating that at this current density, the active materials can be almost fully (de-)lithiated, and so the reaction is considered to be limited by lithium transport within the electrolyte, which is more pronounced in thicker electrodes. As no concentration gradient is expected in the solid electrolyte ( $t_{Li^+} \sim 1$ ), lithium transport in the electrode layer is dominated by ohmic effects. Furthermore, consistent with the reaction zone model, the slopes of the discharge curves are independent of the electrode thickness, but are strongly dependent on the ionic conductivity of the electrolyte. This can be clearly observed upon the use of cathode layers exhibiting different conductivities (Figure 2(d)).

The rate capability tests were then merged in the current-capacity plot shown in Figure 3.

Although at a low current density the theoretical capacity based on the electrode thickness can be discharged, we found that the dischargeable capacity was both thickness-independent and current-dependent, forming a straight line with a slope of -1 at large current densities. Indeed, this is typical behavior of an ohmic-limited electrode system.<sup>18,19</sup>

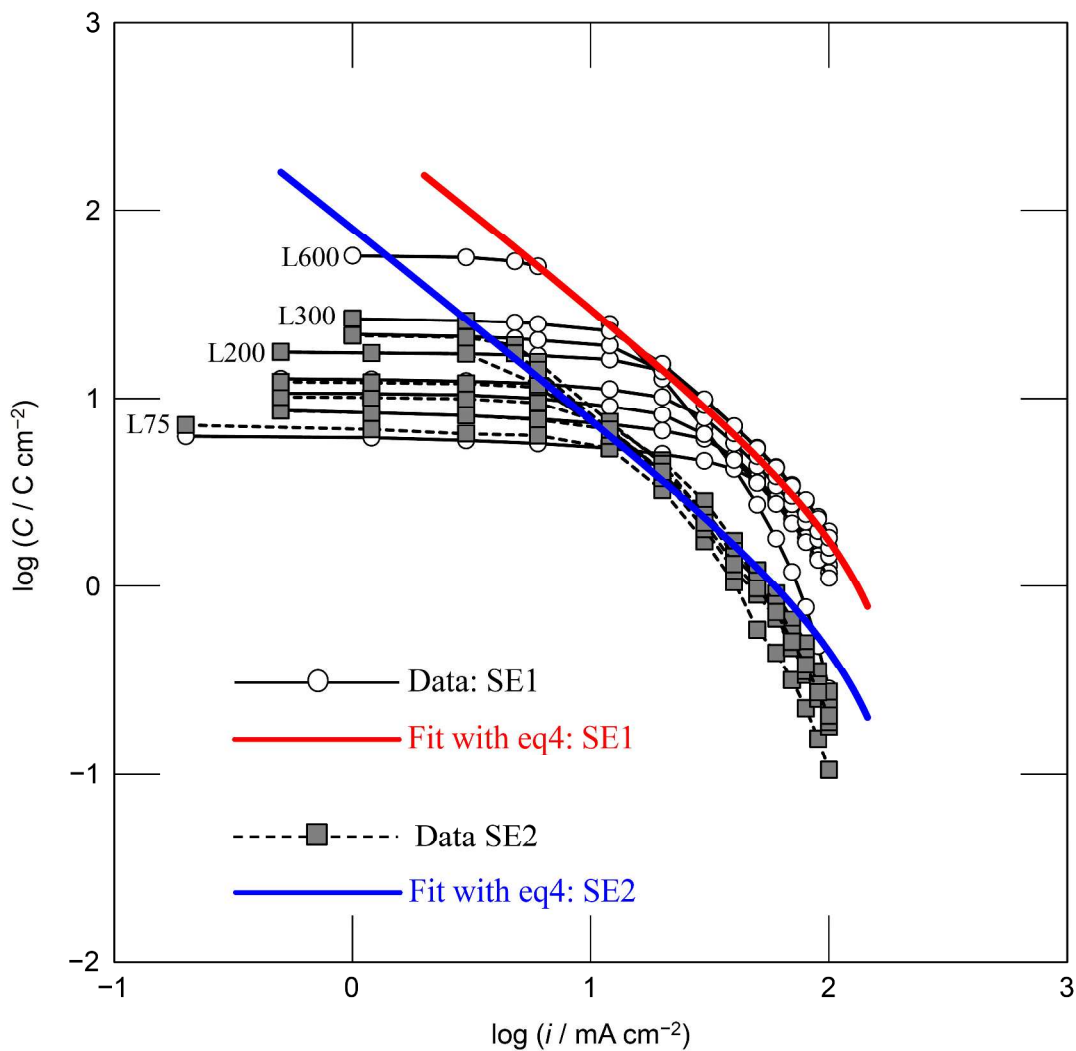


**Figure 3.** Capacity-rate plots for the all-solid-state cells for electrodes L75–L600 at an applied current range of 0.1–100 mA cm<sup>−2</sup>. Fitting was carried out using Eq. 4 and the value of

$\left(\frac{1}{q_c \kappa_{\text{eff},c_j}} + \frac{1}{q_a \kappa_{\text{eff},a}}\right)^{-1}$  was estimated for each system.

Using the cut-off voltage  $V_{\text{cutoff}}$ , the capacity at the ohmic limit condition is defined as:

$$C = t_d i = \frac{1}{i} \times \left( \frac{1}{q_c \kappa_{\text{eff}_{cj}}} + \frac{1}{q_a \kappa_{\text{eff}_{fa}}} \right)^{-1} (U_c^\theta - U_a^\theta - V_{\text{cutoff}} - R_o i) \quad (\text{Eq. 4})$$

where  $t_d$  is the time at which the cell voltage reaches  $V_{\text{cutoff}}$ . The subscript  $j$  corresponds to either SE1 ( $j=1$ ) or SE2 ( $j=2$ ), and the values of the various constants are listed in Table 4. We then wished to extract information regarding the electrode morphology from Figure 3. At a current of  $i \ll (U_c^\theta - U_a^\theta - V_{\text{cutoff}})/R_s$ , the capacity is inversely proportional to the current density, and it is favorable to use a small current density in addition to a thick electrode to minimize the effect of diffusion in the electrode particles. Thus, the value of  $\left( \frac{1}{q_c \kappa_{\text{eff}_{cj}}} + \frac{1}{q_a \kappa_{\text{eff}_{fa}}} \right)^{-1}$  can be extracted for each electrolyte system by fitting with the experimental data (see Figure 3), where the deviation observed at large current densities is caused by the effect of diffusion in the electrode particles. Considering that the cathode layer morphologies are comparable for SE1 and SE2 (see Fig. S6; i.e.,  $\tau_{c1}=\tau_{c2}$ ), the effective conductivities  $\kappa_{\text{eff}_{c1}}$ ,  $\kappa_{\text{eff}_{c2}}$ , and  $\kappa_{\text{eff}_{fa}}$  can be determined and the tortuosity factor  $\tau$  can be estimated, as indicated in Table 5. It should be noted that although estimation of the tortuosity tends to be challenging due to the complex battery reactions taking place,<sup>20–22</sup> a simplified electrochemical treatment of the all-solid-state cells due to the absence of a concentration gradient allows this value to be determined relatively easily.

**Table 4.** Cell parameters for the prepared all-solid-state batteries

$q_c/\text{C cm}^{-3}$	953
$q_a/\text{C cm}^{-3}$	1298

$U_c^\theta/V$ (vs Li/Li <sup>+</sup> )	4.1
$U_a^\theta/V$ (vs Li/Li <sup>+</sup> )	0.1
$V_c/V$	2.5
$R_o/\Omega\text{ cm}^2$	8

**Table 5.** Obtained values for ionic transportation in the electrode layers

$\kappa_{\text{eff\_c1}}/\text{mS cm}^{-1}$	0.73
$\kappa_{\text{eff\_c2}}/\text{mS cm}^{-1}$	0.065
$\kappa_{\text{eff\_a}}/\text{mS cm}^{-1}$	0.21
$\tau_{\text{c1}} (= \tau_{\text{c2}})$	2.47
$\tau_{\text{a}}$	3.32

These results suggest that the tortuosity factor of the anode layer was larger than that of the cathode layer, thereby indicating that ionic transport is less effective in the anode layer. Interestingly, the cross-sectional scanning electron microscopy (SEM) image (Figure S6) showed that graphite was significantly deformed and spread vertically through the sample, likely due to the combination of the layered structure and the strong shear force during mortar mixing. This is unfavorable in the context of ion transport. In contrast, the hard ceramic LiCoO<sub>2</sub> particles appear relatively well dispersed in the composite layer, thereby resulting in a lower tortuosity factor than that of the anode layer. In addition, voids and cracks were observed in the solid electrolyte regions of both of the cathode and the anode, which also lead to interference of ion transfer and an increase in the tortuosity factor. Such interference is a fundamental characteristic of all-solid-state batteries, and its effect on tortuosity should be carefully analyzed. Furthermore, an

improved understanding and control of crack evolution is desirable when considering the application of such systems, thereby indicating the importance of electrode processing and pressure control during operation.

The impedance spectra of our cells (L300 and L600 with SE1) are shown in Figure 4. More specifically, the Nyquist plots (Figure 4(a)) show a small semicircle at high frequencies ( $10^6$  to  $10^1$  Hz), an approximately  $45^\circ$  slope at intermediate frequencies ( $\sim 10^{-3}$  Hz), and capacitive behavior at low frequencies ( $\sim 10^{-4}$  Hz). The dependence on the electrode thickness at mid- and low-frequencies is not usual for conventional charged full cell systems, which tend to have thin electrode layers comparable to the active material particle sizes.<sup>23</sup> However, in our system, the diffusion time constant in the porous electrode is comparable to or greater than those of the active particles due to the presence of a thick electrode and the high diffusion characteristics of the active materials (i.e., ohmic-limited conditions). As such, integration of the finite space Warburg impedance<sup>23–25</sup> (FSW; representing mass transportation in an active material) into the transmission line model<sup>26–29</sup> (TLM; representing mass transport in a porous electrode) would be necessary to model the spectrum presented in Figure 4. The equivalent circuit shown in Figures 4(d) and 4(e) was then employed for simulation of the spectra (see Supporting Information), where the effective conductivity values outlined in Table 5 were used, and all parameters required for FSW were obtained either experimentally or from the literature.<sup>23,30,31</sup> Only the values of  $R_{\text{sep}}$ ,  $R_{\text{CT}}$ , CPE and the numbers of each element per unit volume (N) were refined. The impedance spectra could be explained by the model at all frequency ranges (i.e., Figures 4(a), 4(b), and 4(c)), and the parameters employed for the simulations are listed in Table S1. The good fit of the impedance data also confirms the accuracy of the effective conductivity or tortuosity factors obtained from the rate-capacity plots.

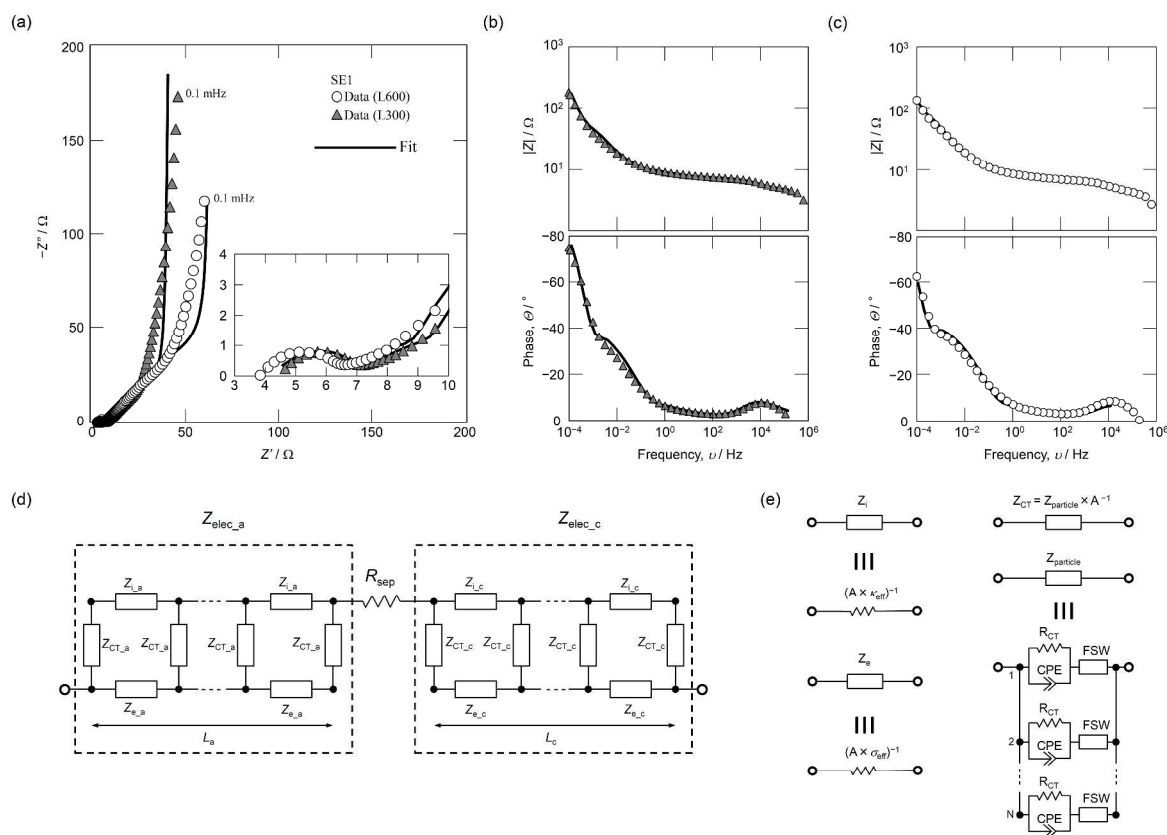


**Figure 4.** Impedance spectroscopy of the all-solid-state cells at 4.1 V: (a) Nyquist plots, (b) and (c) Bode plots. (d) and (e) The equivalent circuit used for the simulation.

Thus, using Eq. 4, the effect of the tortuosity factor or the ionic conductivity on the performance of all-solid-state cells can be quantitatively discussed. Indeed, two modified cases are plotted in Figure S7, namely an improvement in tortuosity (homogeneous mixing, no cracks or voids, expressed by the Bruggeman tortuosity factor  $\tau = \varepsilon^{-0.5}$ ), and an improvement in conductivity ( $10 \text{ mS cm}^{-1}$  for both the anode and cathode layers). As indicated, tortuosity has an impact on battery performance. For example, a doubling of the capacity can be achieved using SE1 at  $i = 20 \text{ mA cm}^{-2}$  for the homogeneously mixed system, again indicating the importance of



electrode processing. More specifically, the battery performance can be significantly improved by altering the mixture conditions employed and by suppressing void formation in the electrode through sintering or hot pressing, although the occurrence of undesired side-reactions must be considered during such processes. Considering the cycle life, pressure control would also be required to suppress crack and void formation during operation.

Conductivity also had a significant influence on battery performance, with an increase in conductivity at the anode producing an enhancement in battery performance. In theory, the full capacity of the L600 configuration ( $15.8 \text{ mAh cm}^{-2}$ ) can be discharged at  $30 \text{ mA cm}^{-2}$  with an electrolyte of  $10 \text{ mS cm}^{-1}$ . Although a few materials exhibiting values  $>10 \text{ mS cm}^{-1}$  have been reported,<sup>8,13,32,33</sup> these materials demonstrate exceptional conductivities at densified conditions achieved either by sintering or hot pressing, thereby suggesting that materials exhibiting high conductivities in the compressed state are desirable for thick electrode all-solid-state battery systems.

In summary, a thick electrode all-solid-state lithium-ion battery containing a  $600 \text{ }\mu\text{m}$ -thick cathode was successfully prepared and operated at room temperature. We found that this system can be accurately described in the context of ohmic limits. In addition, following systematic capacity-current experiments and analysis, we extracted key morphologic parameters for the tortuosity factor, a value that is normally difficult to estimate. Furthermore, the effects of the ionic conductivity and the tortuosity factor on battery performance were quantitatively analyzed. We believe this study can provide guidance in the context of electrode design for developing high performance all-solid-state batteries.

ASSOCIATED CONTENT

**Supporting Information.** Figure S1-S7 and Table S1 is in Supporting Information. The experimental set-up is described in the supporting information and experimental procedures are outlined.

AUTHOR INFORMATION

Corresponding author: Yuki Kato (yuki\_katoh@mail.toyota.co.jp)

**Notes.** The authors declare no competing financial interests.

ACKNOWLEDGMENT

The authors thank Ms. Marta Cazorla Soult and Ms. Poonam Yadav for their support in solid electrolyte synthesis and cell fabrication.

## REFERENCES

- (1) Moshtev, R.; Johnson, B.; State of the Art of Commercial Li ion Batteries. *J. Power Sources* **2000**, *91*, 86–91.
- (2) Hu, L.; Mantia, F. L.; Wu, H.; Xie, X.; McDonough, J.; Pasta, M.; Cui, Y. Lithium-Ion Textile Batteries with Large Areal Mass Loading. *Adv. Energy. Mater.* **2011**, *1*, 1012–1017.
- (3) Evanoff, K.; Khan, J.; Balandin, A. A.; Magasinski, A.; Ready, W. J.; Fuller, T. F.; Yushin, G. Towards Ultrathick Battery Electrodes: Aligned Carbon Nanotube–Enabled Architecture. *Adv. Mater.* **2012**, *24*, 533–537.
- (4) Singh, M.; Kaiser, J.; Hahna, H. Thick Electrodes for High Energy Lithium Ion Batteries. *J. Electrochem. Soc.* **2015**, *162*, A1196–A1201.
- (5) Gallagher, K. G.; Trask, S. E.; Bauer, C.; Woehrle, T.; Lux, S. F.; Tschech, M.; Lamp, P.; Polzin, B. J.; Ha, S.; Long, B.; Wu, Q.; Lu, W.; Dees, D. W.; Jansena, A. N. Optimizing Areal Capacities through Understanding the Limitations of Lithium-Ion Electrodes. *J. Electrochem. Soc.* **2016**, *163*, A138–A149.
- (6) Fuller, T. F.; Doyle, M.; Newman, J. Simulation and Optimization of the Dual Lithium Ion Insertion Cell. *J. Electrochem. Soc.* **1994**, *141*, 1–10.
- (7) Arora, P.; Doyle, M.; Gozdz, A. S.; White, R. E.; Newman, J. Comparison between Computer Simulations and Experimental Data for High-rate Discharges of Plastic Lithium-ion Batteries *J. Power Sources* **2000**, *88*, 219–231.
- (8) Kato, Y.; Hori, S.; Saito, T.; Suzuki, K.; Hirayama, M.; Mitsui, A.; Yonemura, M.; Iba, H.; Kanno, R. High-power All-solid-state Batteries using Sulfide Superionic Conductors. *Nat. Energy* **2016**, *1*, 16030.
- (9) Kubanska, A.; Castro, L.; Tortet, L.; Dollé, M.; Bouchet, R. Effect of Composite Electrode Thickness on the Electrochemical Performances of All-solid-state Li-ion Batteries. *J. Electroceram.* **2017**, <https://doi.org/10.1007/s10832-017-0088-8>.

- (10) Zhang, W.; Leichtweiß, T.; Culver, S. P.; Koerver, R.; Das, D.; Weber, D. A.; Zeier, W. G.; Janek, J. The Detrimental Effects of Carbon Additives in  $\text{Li}_{10}\text{GeP}_2\text{S}_{12}$ -Based Solid-State Batteries. *ACS Appl. Mater. Interfaces*. **2017**, 18–19, 35888–35896.
- (11) Sakuda, A.; Hayashi, A.; Tatsumisago, M. Interfacial Observation between  $\text{LiCoO}_2$  Electrode and  $\text{Li}_2\text{S-P}_2\text{S}_5$  Solid Electrolytes of All-Solid-State Lithium Secondary Batteries Using Transmission Electron Microscopy. *Chem. Mater.* **2010**, 22, 949–956.
- (12) Ohtomo, T.; Hayashi, A.; Tatsumisago, M.; Tsuchida, Y.; Hama, S.; Kawamoto, K. All-Solid-state Lithium Secondary Batteries using the  $75\text{Li}_2\text{S-}25\text{P}_2\text{S}_5$  Glass and the  $70\text{Li}_2\text{S-}30\text{P}_2\text{S}_5$  Glass-ceramic as Solid Electrolytes. *J. Power Sources* **2013**, 233, 231–235.
- (13) Kamaya, N.; Homma, K.; Yamakawa, Y.; Hirayama, M.; Kanno, R.; Yonemura, M.; Kamiyama, T.; Kato, Y.; Hama, S.; Kawamoto, K.; Mitsui, A. A Lithium Superionic Conductor. *Nat. Mater.* **2011**, 10, 682–686.
- (14) Mizuno, F.; Hayashi, A.; Tadanaga, K.; Tatsumisago, M. High Lithium Ion Conducting Glass-Ceramics in The System  $\text{Li}_2\text{S-P}_2\text{S}_5$ . *Solid State Ionics* **2005**, 177, 2721–2725.
- (15) Takada, K.; Inada, T.; Kajiyama, A.; Sasaki, H.; Kondo, S.; Watanabe, M.; Murayama, M.; Kanno, R. Solid-state Lithium Battery with Graphite Anode. *Solid State Ionics* **2003**, 158, 269–274.
- (16) Ohta, N.; Takada, K.; Sakaguchi, I.; Zhang, L.; Ma, R.; Fukuda, K.; Osadam M.; Sasaki, T.  $\text{LiNbO}_3$ -coated  $\text{LiCoO}_2$  as Cathode Material for All Solid-state Lithium Secondary Batteries. *Electrochem. Commun.* **2007**, 9, 1486–1490.
- (17) Oh, G.; Hirayama, M.; Kwon, O.; Suzuki, K.; Kanno, R. Bulk-Type All Solid-State Batteries with 5 V Class  $\text{LiNi}_{0.5}\text{Mn}_{1.5}\text{O}_4$  Cathode and  $\text{Li}_{10}\text{GeP}_2\text{S}_{12}$  Solid Electrolyte. *Chem. Mater.* **2016**, 28, 2634–2640.
- (18) Doyle, M.; Newman, J. Modeling the Performance of Rechargeable Lithium-Based Cells: Design Correlations for Limiting Cases. *J. Power Sources* **1995**, 54, 46–51.

- (19) Doyle, M.; Newman, J. Analysis of Capacity±Rate Data for Lithium Batteries Using Simplified Models of the Discharge Process. *J. Appl. Electrochem.* **1997**, *27*, 846–856.
- (20) Fongy, C.; Jouanneau, S.; Guyomard, D.; Badot, J. C.; Lestriez, B. Electronic and Ionic Wirings Versus the Insertion Reaction Contributions to the Polarization in LiFePO<sub>4</sub> Composite Electrodes. *J. Electrochem. Soc.* **2010**, *157*, A1347–A1353.
- (21) Fongy, C.; Gaillot, A-C.; Jouanneau, S.; Guyomard, D.; Lestriez, B. Ionic vs Electronic Power Limitations and Analysis of the Fraction of Wired Grains in LiFePO<sub>4</sub> Composite Electrodes. *J. Electrochem. Soc.* **2010**, *157*, A885–A891.
- (22) Fongy, C.; Jouanneau, S.; Guyomard, D.; Lestriez, B. Carbon Nanofibers Improve Both the Electronic and Ionic Contributions of the Electrochemical Performance of Composite Electrodes. *J. Power Sources.* **2011**, *196*, 8494–8499.
- (23) Levi, M. D.; Aurbach, D. Frumkin Intercalation Isotherm – A Tool for the Description of Lithium Insertion into Host Materials: A Review. *Electrochim. Acta* **1999**, *45*, 167–185.
- (24) Buck, R. P. Diffusion-migration Impedances for Finite, One-dimensional Transport in Thin Layer and Membrane Cells: An Analysis of Derived Electrical Quantities and Equivalent Circuits. *J. Electroanal. Chem.* **1986**, *210*, 1–19.
- (25) Franceschetti, D. R.; Macdonald, J. R. Small-Signal A-C Response Theory for Electrochromic Thin Films. *J. Electrochem. Soc.* **1982**, *129*, 1754–1756.
- (26) Tröltzsch, U.; Kanoun, O. Generalization of Transmission Line Models for Deriving the Impedance of Diffusion and Porous Media. *Electrochim. Acta.* **2012**, *75*, 347–356.
- (27) Ogihara, N; Itou, Y; Sasaki, T; Takeuchi, Y. Impedance Spectroscopy Characterization of Porous Electrodes under Different Electrode Thickness Using a Symmetric Cell for High-Performance Lithium-Ion Batteries. *J. Phys. Chem. C* **2015**, *119*, 4612–4619.
- (28) Malifarge, S.; Delobel, B.; Delacourt, C. Determination of Tortuosity Using Impedance Spectra Analysis of Symmetric Cell. *J. Electrochem. Soc.* **2017**, *164*, E3329–E3334.

- (29) Siroma, Z.; Sato, T.; Takeuchi, T.; Nagai, R.; Ota, A.; Ioroi, T. AC impedance analysis of ionic and electronic conductivities in electrode mixture layers for an all-solid-state lithium-ion battery. *J. Power Sources* **2017**, *316*, 215–223.
- (30) Persson, K.; Sethuraman, V. A.; Hardwick, L. J.; Hinuma, Y.; Meng, Y. S.; van der Ven, A.; Srinivasan, V.; Kostecki, R.; Ceder, G. Lithium Diffusion in Graphitic Carbon. *J. Phys. Chem. Lett.* **2010**, *1*, 1176–1180.
- (31) Xia, H.; Lu, L.; Ceder, G. Li Diffusion in LiCoO<sub>2</sub> Thin Films Prepared by Pulsed Laser Deposition. *J. Power Sources*, **2006**, *159*, 1422–1427.
- (32) Sun, Y.; Suzuki, K.; Hori, S.; Hirayama, M.; Kanno, R. Superionic Conductors: Li<sub>10+δ</sub>[Sn<sub>y</sub>Si<sub>1-y</sub>]<sub>1+δ</sub>P<sub>2-δ</sub>S<sub>12</sub> with a Li<sub>10</sub>GeP<sub>2</sub>S<sub>12</sub>-type Structure in the Li<sub>3</sub>PS<sub>4</sub>–Li<sub>4</sub>SnS<sub>4</sub>–Li<sub>4</sub>SiS<sub>4</sub> Quasi-ternary System. *Chem. Mater.* **2017**, *29*, 5858–5864.
- (33) Seino, Y.; Ota, T.; Takada, K.; Hayashi, A.; Tatsumisago, M. A Sulphide Lithium Super Ion Conductor is Superior to Liquid Ion Conductors for Use in Rechargeable Batteries. *Energy Environ. Sci.* **2014**, *7*, 627–631.